

Examining the utility of pinhole-type screens for lightfield display

P. KOPYCKI,¹ A. TOLOSA,² M. J. LUQUE,¹  M. C. GARCIA-DOMENE,¹ M. DIEZ-AJENJO,¹ G. SAAVEDRA,¹ AND M. MARTINEZ-CORRAL^{1,*} 

¹Department of Optics and Optometry and Visual Sciences, University of Valencia, E46100 Burjassot, Spain

²DoitPlenoptic S.L., Parc Científic de la Universitat de València, E-46980 Paterna, Spain

*manuel.martinez@uv.es

Abstract: The use of microlens arrays for lightfield display has the drawback of providing images with strong chromatic aliasing. To overcome this problem, pinhole-type lightfield monitors are proposed. This paper is devoted to evaluating the capability for such lightfield monitors to offer the user a convincing 3D experience with images with enough brightness and continuous aspect. Thus, we have designed a psychophysical test specifically adapted for lightfield monitors, which allowed us to confirm the usability of pinhole-type monitors.

© 2021 Optical Society of America under the terms of the [OSA Open Access Publishing Agreement](#)

1. Introduction

Lightfield imaging is a technique that allows the capture and display of 3D information from 3D scenes obtained either from computer simulations or from the real world [1–8]. Apart from the display of 3D scenes, lightfield imaging has many useful applications such as, for example, obtaining depth maps, performing digital refocusing, removing occlusions, or making object recognition [4–8].

In lightfield systems, a 2D array of 2D elemental images of a given surface 3D object is generated by a microlens array and recorded by a CCD. Each elemental image shows a different perspective of the 3D object. The recorded elemental images are displayed by an optical device, such as an LCD, in front of another microlens array to reconstruct the 3D image. Other possibilities for capturing the lightfield image are the use of plenoptic cameras or the synthetic-aperture method in which a single digital camera is set on a moving platform. A good but low-resolution method is to use a Kinect device, which allows the capture of RGB and depths maps, and from them the collection of elemental images [9].

During the past few years many methods of displaying lightfield images were developed. The first and obvious way is to place a microlens array in front of a monitor [10]. However, among other problems, the limited viewing angle caused by the properties of microlenses was a significant drawback. To alleviate it, different methods were developed [11,12]. Another major issue is the chromatic aliasing that occurs in the display of non-monochromatic images [13]. In any kind of color displays; like those in phones, tablets, computers or TVs, any white pixel is indeed composed by several, commonly three, monochromatic sub-pixels. This fact can give rise to chromatic aliasing since the red (or green or blue) subpixels subtend all the same angle as seen from the optical centers of the microlenses. For this reason, microlens-based lightfield monitors are not convenient when displaying polychromatic images [14].

One method for avoiding chromatic aliasing is the use of pinhole arrays instead of microlenses [15–17]. Pinholes do not have any refraction power, so that the effect of chromatic aliasing cannot occur. Besides, the viewing angle can be set at will since it is determined by the distance between the pinhole array and the display pixels [18]. Despite these advantages, there is still one essential question that must be investigated; is there any optimum value for the pinhole size

that allows the observers to have a sufficient 3D experience? The question comes out from the fact that to provide an accurate 3D reconstruction, the pinholes should be as small as possible. However, small pinholes give rise to dotted-like display aspect, and to images with very low brightness. Although these features are known, it is highly surprising that, at the best of our knowledge, no study has been reported aiming to link the pinhole aperture with the 3D capability, and consequently to find the optimum configuration in terms of 3D effect and brightness.

In this paper we aim to confirm the utility of pinhole arrays for effective lightfield display. To this end we have designed a psychophysical test specifically adapted for lightfield monitors, based on stereoacuity measurements using modified binary search (MOBS) [19], to examine the 3D capability of pinhole-type monitors. The stereoacuity measurements of a group of young subjects have been used to test it and to find out the range of pinhole sizes that provides the best 3D perception for a given pinhole pitch. The rationale behind the experiment is that, for a sample of subjects with normal stereoscopic vision, poorer 3D simulations would be linked to impaired depth perception, resulting in reduced ability to detect small depth changes and, therefore, in worse stereoacuity. Although our results have been obtained for a given lightfield monitor, built from a seven-inches tablet that is set 1 meter away from the observer, the extension of our result to any other geometry, such as large-area displays, for instance, is immediate.

2. Lightfield monitor

In lightfield technology, 3D images are displayed by lightfield monitors, which are autostereoscopic, i.e. they do not require the use of any type of special glasses, and have the advantage of displaying polychromatic 3D images with full parallax. The most important feature is that they reproduce, properly scaled, the light distribution of the original 3D scene. Since the observer can adjust her/his accommodation and visual-axes convergence to that light distribution, the convergence-accommodation conflict is avoided [6–8]. In order to set up a conventional lightfield monitor, an array of microlenses (MLA) is placed in front of a pixelated screen (LCD, OLED, AMOLED, etc.) in such a way that the pixels are at the focal plane of the microlenses, and therefore their images are formed at the infinite. In a common realization of a lightfield monitor, just behind each microlens a microimage is displayed, so that both the microlens and the microimage have the same size. The microimages can be obtained directly with a plenoptic camera or transformed from the elemental images captured with an array of digital cameras [9,15,16].

Once the microimages are displayed on the pixelated display, the microlenses integrate the light rays emitted by the pixels, forming a luminous 3D image. But the problem comes from the fact that any microlens has its own optical center so that light from different sub-pixels is refracted to different directions (see Fig. 1).

In a real case each microlens covers many pixels, and therefore many sub-pixels. This provides an apparent chromatic aliasing because the light beams proceeding from individual sub-pixels of same color are refracted towards the same direction.

To illustrate this effect, we have prepared a real example of chromatic aliasing. First, in Fig. 2(a) we show the lightfield image (i.e., collection of microimages) that is projected on the pixelated monitor (Samsung tablet with 288 ppi). Each microimage is composed by 17×17 pixels. To build the lightfield monitor, we used a microlens array that was placed at the focal-length distance from the pixels and aligned with the microimages. The microlenses pitch was $p = 1.0 \text{ mm}$ and the focal length $f = 3.0 \text{ mm}$ (Fresneltech, model 630). In Fig. 2(b) we show the displayed image as perceived by a monocular observer placed in front of the lightfield monitor. In this image we can see chromatic patches that follow a periodic pattern. Clearly, this chromatic effect is more intense in the white zones of the scene, and almost imperceptible in the monochromatic zones, like the green tree or the red pants. Note, however, that when observing the outer part of the screen (for example the upper right corner) this effect is less apparent. This is because the

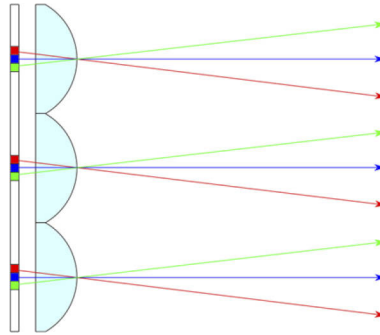


Fig. 1. Light passing through the microlens from individual sub-pixels. As can be seen, the amount of light of a given color depends on observation angle. For simplicity, the picture shows only 3 sub-pixels per microlens.

eye (in this case the camera) is receiving from those points non-paraxial rays, and therefore the proportionality between the inclination angle of received rays and the lateral position of emitting sub-pixels is lost.

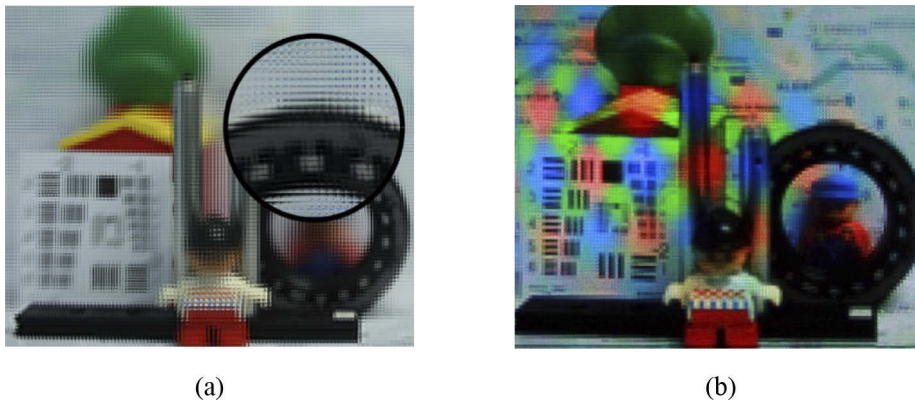


Fig. 2. Real example of chromatic aliasing when the lightfield monitor is equipped with an MLA. (a) The collection of microimages, i.e. the lightfield image, projected onto the pixelated tablet; (b) Displayed 3D image as seen by a monocular observer placed in front of the lightfield monitor.

The easiest way of avoiding chromatic aliasing is to equip the lightfield monitor with a pinhole array instead of an MLA. We show in Fig. 3 an example of the image provided by such lightfield architecture. For this example, we have used the same lightfield image as in Fig. 2 but substituted the MLA by a pinhole array with pitch $p = 1.0 \text{ mm}$.

Additionally, in [Visualization 1](#) we show a movie whose frames have been captured by moving laterally the photography camera. This movie confirms that the pinholed lightfield monitor provides the observer with different perspectives depending on her/his position.

Clearly, pinholes solve the chromatic aliasing issue. However essential questions are still open: does this monitor offer convincing 3D experience? do images have enough brightness? or, is the aspect of the 3D images continuous?



Fig. 3. Displayed 3D image as seen by a monocular observer (a photography camera in our experiment) placed in front of the lightfield monitor. In [Visualization 1](#) we can observe the parallax of such image.

3. Experimental setup

To provide an answer to those questions, we have designed a test to measure the stereoscopic acuity based on the classic Howard-Dolman test [20]. The test is composed by two equal, vertical narrow, plane bright rods against a black uniform background, generated using a tablet and different pinhole array. The rods' lightfield images have been calculated to ensure that, after the light from the display has gone through the pinholes, the left-side rod (reference or fixed rod) is reconstructed just at the pinholes plane. The right-side rod (test), however, is rendered at a variable distance in front or behind that plane. The borders of the reference rod were blurred to match both rods in angular size and to disguise the fact that the mobile rod would appear unfocused at every plane except the reference plane. Besides avoiding these monocular depth clues, blur helped to make the size changes between consecutive trials less visible, avoiding thus a possible bias in the observer response. The generation procedure is described in detail in Section 4.

As in the Howard-Dolman test, we determine with our device the maximum disparity, δ , that allows both rods to be perceived as belonging to the same frontal plane.

$$\delta = \frac{IPD \cdot \Delta x}{r^2} \quad (1)$$

where Δx is the threshold distance between the planes containing the reference and test rods, r is the distance between the observer and the plane containing the reference rod and IPD is the observer's interpupillary distance. δ is a measurement of stereoacuity, with lower values indicating better acuity. The rationale of the experiment is that more realistic 3D images will be related with better stereoacuity.

To measure the threshold distance Δx , we adapted the modified binary search (MOBS) psychophysical method [19]. The observer's task consists in describing the test rod position relative to the reference rod, using the terms "nearer" and "farther". The available range of positions of the test rod (total range of the device) is [-6, 6] cm around the reference rod. This range is determined by the need to avoid overlapping of the two rods and the convenience of disposing of a symmetrical interval.

At each trial, a working interval is defined by two planes where the observer should perceive the mobile rod nearer (front boundary FB) or farther (back boundary BB) than the reference rod. To randomize the starting point, the initial values of these limits covers only $\frac{3}{4}$ of the total range of the device and are decided by showing initially to the observer both rods in the same plane; if the subject answers "nearer", the FB and BB planes are placed at the maximum and at half the

device capacity, respectively $([-6,3] \text{ cm})$; if the answer is “farther”, the BB and FB planes are placed at maximum and at half the capacity of the device $([-3,6] \text{ cm})$.

The test stimulus is always placed at the middle of the working interval. According to the subject’s response, this position replaces the corresponding extreme of the working interval (FB if “nearer” and BB if “farther”) and the procedure is repeated with the new interval (Fig. 4). In this way, the working interval is narrowed, until a region where both rods appear at the same plane is found.

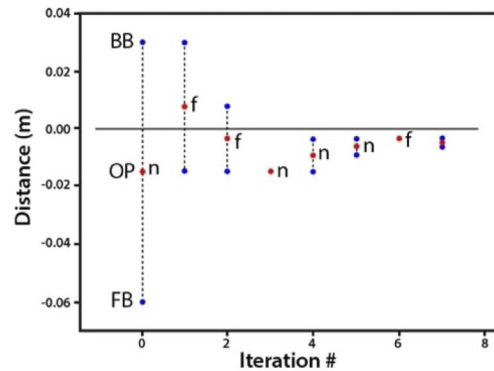


Fig. 4. Example measurement sequence. Boundaries of the working intervals in normal trials are marked as blue dots, test positions are marked by the red dots. Single red dots indicate checking points. Observer’s responses are reported as “n” (“nearer”) and “f” (“farther”). Note that the trial for choosing the initial working interval is not shown.

Checking trials are introduced after two consecutive responses of the same sign, by presenting the rod at the working interval boundary of the opposite sign (FB if the response is “farther” and BB if “nearer”, see iterations 3# and 6# in Fig. 4). If the subject’s response is consistent, the measurement continues, if not, the working interval is reverted to the previous step.

The measurement ends when one of the following termination criteria is met: 1) two wrong answers at a given checking point, 2) a sampling range narrower than 5% of the system’s total measuring range or 3) a distance between the two rod planes below the resolution limit of the device (1 mm). The observer’s threshold is the middle point of the last interval.

4. Image generation

The first step for implementing our procedure is to prepare an algorithm that allows the generation in real time of the corresponding lightfield images. The algorithm is based on the scheme shown in Fig. 5. To understand this scheme is necessary to remember that in a lightfield monitor, any pixel carries the spatial-angular information of a light ray (in fact of a narrow light beam). The spatial information is determined by the position of the centre of the pinhole (or the centre of the microlens in case of MLA-based lightfield monitor). The angular content is determined by the slope of the straight line that connects the centre of the pixel and the centre of the pinhole.

Using this concept, we can calculate the lightfield image corresponding to a given position of the right rod. A schematic representation of the algorithm is shown in Fig. 5. The scheme shows only the (x, z) meridian section, since the result is independent on y . In the figure we see the LED array, the pinhole array, and the rod. In our experiment we use two rods, but is more convenient to project first one rod, then to project the second rod and later to sum both images. All we must do is to project onto the LED panel, through any pinhole of the array, the two lateral edges of the rod. We use the point O as the origin of the coordinate system. In practice, for every pinhole, we must calculate two values: x_{i1} and x_{i2} (i refers to the pinhole index). We take one pixel as

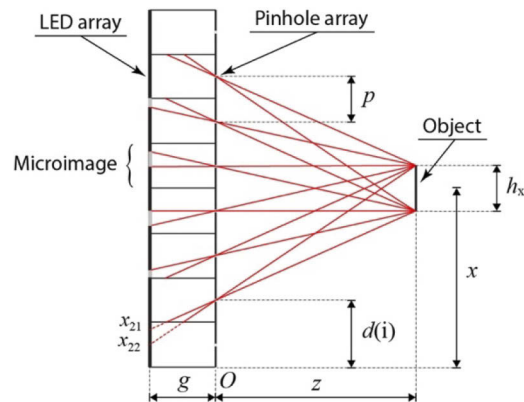


Fig. 5. Lightfield image generation. The scheme shows a (x, z) meridian section. Each pinhole has associated one microimage. Note that in our experiment rods are plane objects with width h_x and height h_y . The height of the rod covers the vertical size of the tablet.

the distance unit for the algorithm. Thus, our algorithm will work for every monitor by simply changing the value of pixel size in meters. Value g is the gap between the LED panel and the pinhole array, $d(i)$ is distance between the centre of the pinhole and the point O , z is distance between the object and the pinhole array, x is distance between centre of the rod and coordinate axis, h_x is width of the rod, and p is pitch between pinholes. All of those values must be the same as in our real monitor. Then we use the equations:

$$x_{i1} = \frac{x}{z} \left(x - d(i) - \frac{h_x}{2} \right) + d(i) \quad \text{and} \quad x_{i2} = \frac{x}{z} \left(x - d(i) + \frac{h_x}{2} \right) + d(i) \quad (2)$$

As we shown in Fig. 5, the pixels between x_{i1} and x_{i2} should set to white, but we have to take into account the size of the microimage corresponding to that pinhole. Only pixels within the borders of the microimage are set to white. In the example drawn Fig. 5, for pinhole $i = 2$ the two positions are out from the corresponding microimage. Thus, all the microimage is set to black.

After that, and in order to avoid the pseudoscopic effect [21] every microimage is rotated by π radians around its centre, as shown in Fig. 6.

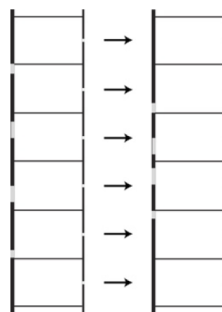


Fig. 6. To avoid the pseudoscopic effect, every microimage is rotated by π around its centre.

In Fig. 7 we show an example of the final lightfield frame. The reference fixed rod is on the left ($z = 0 \text{ mm}$) and the movable test rod on the right ($z = +25 \text{ mm}$). Positive z values mean that the bar is in front of the pinhole array. As we can see, although the lightfield image is calculated for two bars with the same width, the pattern corresponding to the movable bar is much wider than that of the reference bar.

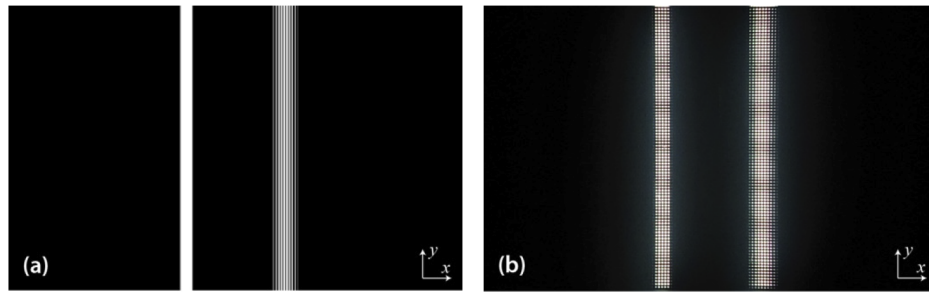


Fig. 7. (a) Calculated lightfield image corresponding to the reference bar at $z = 0$, and the moveable bar at $z = +25$ mm; (b) Image displayed through a pinhole array as seen by a monocular observer placed in front of the lightfield monitor.

As shown in Fig. 7(b) this generates an additional problem: the image of the movable rod provided to the observer by the pinhole array is wider and with blurred borders. This constitutes a monocular clue to the position of the rod. To avoid this drawback, the edges of the mobile rod were blurred, by adding at both sides linear grey-level ramps, so that the width of the pattern equals to that of the movable rod. We can see the resulting lightfield image in Fig. 8.

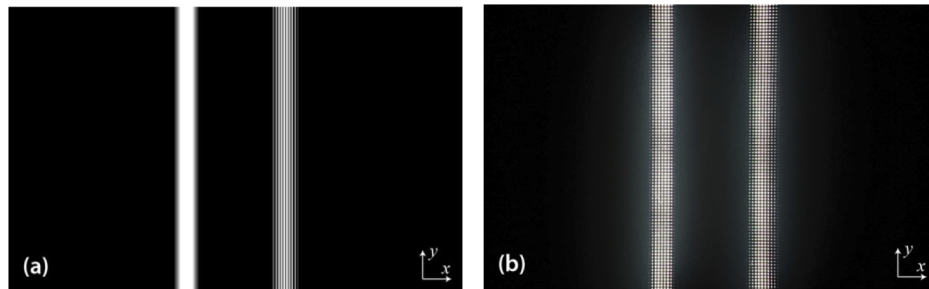


Fig. 8. (a) Same lightfield image as in Fig. 7, but with artificial blur added to the reference rod; (b) Display through the pinhole array.

5. Results

The Howard-Dolman test was implemented using a 2560×1600 pixels (288 ppi) Samsung Galaxy Tab S 10.5 placed at $r = 1$ m from the observer in an otherwise dark room. A chin rest was used to fix observer's head position. We examined four pinhole arrays, all with the same pitch of 1.200×1.200 mm (17×17 pixels per pinhole), but different transparent area: 3×3 , 7×7 , 11×11 and 15×15 pixels per pinhole. The gap g between the pinhole array and the tablet LED array was set to $g = 4$ mm. For these values of pitch and gap, the viewing angle was of 17° . Naturally, reducing the gap could increase this angle.

The lightfield images were calculated so that the two rods were always at the center of the monitor. The width of the rods was $h_x = 5.0$ mm, whereas the distance between rods was set to $2x = 20$ mm. This determines that the depth boundary of the device was 60 mm, since above this value the rods overlap. For computer-tablet connection and image generation and display we used PsychoPy package [22], with the examination algorithm implemented in a Python script.

The pinhole arrays were manufactured by photolithographic means, so that we had four films all with the same pitch but different size for the transparent squares (see Fig. 9). The pinhole arrays were tested in succession in a sample of 19 young observers with normal binocular vision, as

determined by the Random Stereotest. Inclusion criteria were stereoacuity better than 250'' and ability to determine whether the object is "outside" or "inside" the background. The observers, in the 20-25 age range, were students of the Faculty of Physics, University of Valencia, and naïve as to the aim of the experiment.

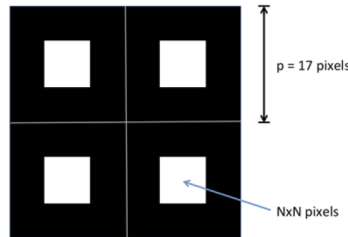


Fig. 9. Subset of the pinhole screen formed by a periodic array of transparent squares.

Data does not follow the normal distribution ($P \leq 0.015$ for all samples in the Shapiro-Wilk test). The results show a trend for worse stereoacuity and larger sample dispersion with increasing transparent area (Fig. 10), indicating lower 3D effect, but though the Friedman's test indicates significant differences between the different pixel arrays ($\chi^2 = 9.972$, $P = 0.019$), Dunn's post-hoc with the Bonferroni correction for multiple comparisons (Table 1) only reveals significant differences between the results for 3×3 and 15×15 ($Z = -1.263$, adjusted $P = 0.015$).

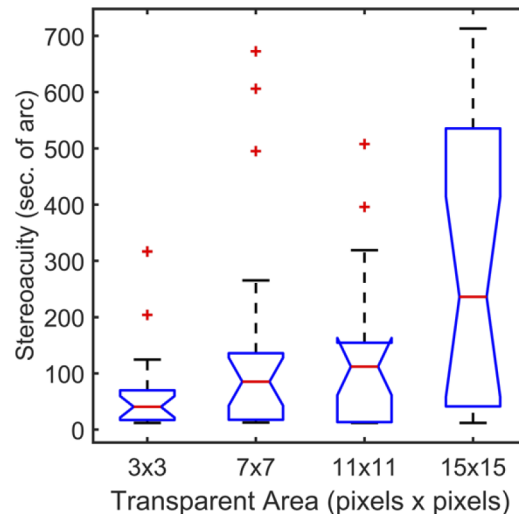


Fig. 10. Stereoacuity distributions for the four pixel array sizes. Red lines: median. Upper and lower boundaries of the box, 25 and 75 percentiles. Whiskers: distribution range. Red markers: Outliers.

The changes in stereoacuity with pixel array size provide a perceptual ranking of the 3D performance of the different pinhole arrays. The results are consistent with what would be expected theoretically, with worse results for the larger pinhole sizes, provided that the reduction in luminance did not affect stereoacuity. This reduction would not be expected in the photopic range [23,24], particularly for the high contrast stimuli in our experimental setting [24], but might appear in the 3×3 array for low luminance tablets. To determine if the performance of any array is acceptable in absolute terms, the stereoacuity values should, at least, be within what would be considered normal in a population with unimpaired 3D vision. This range is strongly dependent

Table 1. Pairwise comparison between the stereoacuity values obtained with different pixel arrays. Each row tests the null hypothesis that the Sample 1 and Sample 2 distributions are the same. Asymptotic significances P (2-sided tests) and Z-scores are displayed. The last column contains the Bonferroni correction. The significance level is 0.05.

Sample 1-Sample 2	Test Statistic	Std. Error	Z score	P-value	Corr. P
3 × 3 vs 7 × 7	-0.500	0.419	-1.194	0.233	1.000
3 × 3 vs 11 × 11	-0.553	0.419	-1.319	0.187	1.000
3 × 3 vs 15 × 15	-1.263	0.419	-3.016	0.003	0.015
7 × 7 vs 11 × 11	-0.053	0.419	-0.126	0.900	1.000
7 × 7 vs 15 × 15	-0.763	0.419	-1.822	0.068	0.411
11 × 11 vs 15 × 15	-0.711	0.419	-1.696	0.090	0.539

on the stimulus and task, but normal values in the age group of this experiment lie within 60-90 seconds of arc [25]. The median values obtained for the 11 × 11 and 15 × 15 arrays would be outside this range. Arrays 3 × 3 and 7 × 7 yield values in the normal range and are therefore the best options. Note that while 3 × 3 pinholes transmit 3.1% of light emitted by the microimages, 7 × 7 pinholes transmit 17%. Thus, even though 3 × 3 yields better stereoacuity, greater image brightness would make 7 × 7 preferable. A larger subject sample would be necessary to confirm whether the differences between these two arrays is statistically significant. Note that currently commercial tablets offer brightness values up to 600 cd/m². In that case, the brightness achievable with the 7 × 7 screen would be around 100 cd/m². This value is larger than brightness values offered by tablets and cell phones in automatic brightness mode in dark surrounds, and is larger than the 80 cd/m² minimum recommended by ISO 9241-307:2008 [26]. This confirms the utility, with the current state of display technology, of pinhole-type lightfield monitors when used in a dark environment.

6. Conclusions

We have evaluated the capability of pinhole-type lightfield monitors to display 3D images. To this end we have designed a psychophysical test and measurement protocol. This has allowed us to demonstrate that pinhole-type monitors offer good stereoacuity with good image brightness. Although this result has been obtained for a given lightfield monitor, its extension to any other geometries is immediate. Thus, we can conclude that the use of pinhole-type monitors is feasible to avoid the chromatic Moiré problems inherent to microlenses-type lightfield monitors.

Funding. Cátedra Alcon-Fisabio-UVEG; Generalitat Valenciana (PROMETEO/2019/048); Ministerio de Ciencia, Innovación y Universidades (RTI2018-099041-B-I00).

Disclosures. The authors declare that there are no conflicts of interest related to this article.

Data availability. Data underlying the results presented in this paper are not publicly available at this time but may be obtained from the authors upon reasonable request.

References

1. G. Lippmann, "Epreuves reversibles donnant la sensation du relief," *J. Phys. Theor. Appl.* **7**(1), 821–825 (1908).
2. E. H. Adelson and J. Y. A. Wang, "Single lens stereo with plenoptic camera," *IEEE Trans. Pattern Anal. Machine Intell.* **14**(2), 99–106 (1992).
3. M. Cho, M. Daneshpanah, I. Moon, and B. Javidi, "Three-dimensional optical sensing and visualization using integral imaging," *Proc. IEEE* **99**(4), 556–575 (2011).
4. J. H. Park, K. Hong, and B. Lee, "Recent progress in three-dimensional information processing based on integral imaging," *Appl. Opt.* **48**(34), H77–H94 (2009).
5. H. Navarro, G. Saavedra, A. Molina, M. Martínez-Corral, R. Martínez-Cuenca, and B. Javidi, "Optical slicing of large scenes by synthetic aperture integral imaging," *Proc. SPIE* **7690**, 7690 (2010).
6. X. Xiao, B. Javidi, M. Martínez-Corral, and A. Stern, "Advances in three-dimensional integral imaging: sensing, display, and applications," *Appl Opt.* **52**(4), 546–560 (2013).

7. H. Navarro, A. Dorado, G. Saavedra, and M. Martínez-Corral, "Three-dimensional imaging and display through integral photography," *J. Inf. Commun. Convergence Eng.* **4**(2), 89–96 (2014).
8. M. Martínez-Corral, A. Dorado, J. C. Barreiro, G. Saavedra, and B. Javidi, "Recent advances in the capture and display of macroscopic and microscopic 3D scenes by integral imaging," *Proc. IEEE* **105**(5), 825–836 (2017).
9. A. Dorado, S. Hong, G. Saavedra, J. C. Barreiro, B. Javidi, and M. Martínez-Corral, "Toward 3D integral-imaging broadcast with increased viewing angle and parallax," *Optics and Lasers in Engineering* **107**, 83–90 (2018).
10. J. Arai, H. Kawai, and F. Okano, "Microlens arrays for integral imaging system," *Appl. Opt.* **45**(36), 9066–9078 (2006).
11. B. Lee, S. Jung, and J. H. Park, "Viewing-angle-enhanced integral imaging by lens switching," *Opt. Lett.* **27**(10), 818–820 (2002).
12. Y. Kim, J. H. Park, H. Choi, S. Jung, S. W. Min, and S. Lee, "Viewing-angle-enhanced integral imaging system using a curved lens array," *Opt. Express* **12**(3), 421–429 (2004).
13. J.-Y. Jang and M. Cho, "Color artifact-free three-dimensional integral imaging display with large depth using a lens array based on sublens structure," *J. Disp. Technol.* **12**(6), 610–615 (2016).
14. H. Sasaki, N. Okaichi, H. Watanabe, T. Omura, M. Kano, and M. Kawakita, "Color Moiré Reduction and Resolution Improvement for Integral 3D Displays Using Multiple Wobbling Optics," *2020 IEEE International Symposium on Mixed and Augmented Reality (ISMAR)*, 2020, pp. 109–116.
15. A. Schwarz, J. Wang, A. Shemer, Z. Zalevsky, and B. Javidi, "Lensless three-dimensional integral imaging using variable and time multiplexed pinhole array," *Opt. Lett.* **40**(8), 1814–1817 (2015).
16. J. Jung, S. Park, Y. Kim, and B. Lee, "Integral imaging using a color filter pinhole array on a display panel," *Opt. Express* **20**(17), 18744–18756 (2012).
17. H. Choi, J. Kim, S. W. Cho, Y. Kim, J. B. Park, and B. Lee, "Three-dimensional–two-dimensional mixed display system using integral imaging with an active pinhole array on a liquid crystal panel," *Appl. Opt.* **47**(13), 2207–2214 (2008).
18. Y. Kim, J. Kim, J. M. Kang, J. H. Jung, H. Choi, and B. Lee, "Point light source integral imaging with improved resolution and viewing angle by the use of electrically movable pinhole array," *Opt. Express* **15**(26), 18253–18267 (2007).
19. R. A. Tyrrell and D. A. Owens, "A rapid technique to assess the resting states of the eyes and other threshold phenomena: The Modified Binary Search (MOBS)," *Behavior Research Methods, Instruments, & Computers* **20**(2), 137–141 (1988).
20. H. J. Howard, "A test for the judgment of distance," *Am. J. Ophthalmol.* **2**(9), 656–675 (1919).
21. H. Navarro, R. Martínez-Cuenca, G. Saavedra, M. Martínez-Corral, and B. Javidi, "3D integral imaging display by smart pseudoscopic-to-orthoscopic conversion (SPOC)," *Opt. Express* **18**(25), 25573–25583 (2010).
22. J. Peirce, J. R. Gray, S. Simpson, M. MacAskill, R. Höchenberger, H. Sogo, E. Kastman, and J. K. Lindeløv, "PsychoPy2: Experiments in behavior made easy," *Behav Res* **51**(1), 195–203 (2019).
23. C. Mueller C, and V. Lloyd, "Stereoscopic Acuity for Various Levels of Illumination," *Proc. Natl. Acad. Sci. U. S. A.* **34**(5), 223–227 (1948).
24. T. Geib and C. Baumann, "Effect of luminance and contrast on stereoscopic acuity," *Graefe's Arch. Clin. Exp. Ophthalmol.* **228**(4), 310–315 (1990).
25. M. E. F. Piano, L. P. Tidbury, and A. R. O'Connor, "Normative Values for Near and Distance Clinical Tests of Stereoacuity," *Strabismus* **24**(4), 169–172 (2016).
26. "International Organization for Standardization. Ergonomics of human-system interaction — Part 307: Analysis and compliance test methods for electronic visual displays," *ISO 9241-307:2008* (2008).